Indian Journal of Chemical Technology
Vol. 33, September 2026, pp. 719-733
DOI: 10.56042/ijct.v33i5.26227

Peristaltically induced pulsating flow of nanofluid in an inclined porous space

G.S.S. Durga Bhavani* & Suripeddi Srinivas

Department of Mathematics, VIT-AP University, Amaravati-522237, India
*E-mail: gssdurgabhavani20@gmail.com

Received 5 December 2025; accepted 9 April 2026

The present study investigates the combined influence of magnetic field, channel inclination, and porous effects on peristaltic-induced pulsatile flow of nanofluid containing metallic nanoparticles. The flow is assumed to occur in a two-dimensional porous inclined channel under the action of an arbitrary periodic pressure gradient. Gold (Au) and Silver (Ag) nanoparticles with a uniform volume fraction of 5% are dispersed in three different base fluids water, blood, and kerosene to examine their comparative thermal and flow characteristics. A perturbation technique with amplitude ratio as a small parameter is employed to obtain analytical expressions for the zero- and first-order velocity and temperature distributions. The graphical results are provided to demonstrate how nanoparticle type, base fluid and particle shape affect the velocity and temperature profiles. Moreover, velocity and temperature distributions along with streamlines and isothermal contours are presented for various parameter variations to visualize the flow patterns and thermal behaviour within the channel. It is further observed that a rise in the Hartman number leads to a reduction in fluid velocity, while a higher wavenumber enhances the temperature distribution. The size of the trapping bolus is also found to enhance with the Grashof number. This study explores how varying nanoparticle shapes and their respective shape factors affect the flow and heat transfer characteristics of a nanofluid, under an external magnetic field. The results show that lamina shaped nanoparticles enhance heat transfer most effectively, while the cylinder shapes display comparatively weaker effects.

Keywords: MHD, Nanofluid, Peristaltic Transport, Porous Medium, Pulsating Flow

Introduction

The process of peristalsis uses the symmetrical contraction and suspension of smooth muscles to move different bodily fluids throughout an organism. In biomedical devices, the peristaltic pumping concept is also used to move liquids without the need for internal moving parts. Peristalsis is fundamental to many physiological processes. A notable example is the blood-circulation pump used in dialysis, which relies on peristaltic motion to efficiently transport blood through the extracorporeal filtration system and remove impurities. Peristalsis of hazardous liquids is used in the nuclear sector to prevent environmental damage[1-5]. Mishra and Rao[2] explored the dynamics of peristaltic transport of a Newtonian fluid in an asymmetric channel configuration. Their results indicate that a symmetric channel exhibits a wider trapping zone and a greater flow rate compared to an asymmetric one. Srinivas and Kothandapani[3] examined peristaltic transport in an asymmetric, inclined channel with permeability effects and found that a rise in the Froude number leads to a reduction in the pressure gradient. Srinivas and Muthuraj[4] analyzed the MHD peristaltic behaviour of a Jeffrey liquid within an inclined asymmetric channel, incorporating slip boundary conditions to capture more realistic wall-fluid interactions. The top wall of a symmetric channel experiences higher stress than that of an asymmetric channel. Devakar *et al*.[5] investigated the influence of an applied magnetic field on the peristaltic motion of a couple-stress fluid in a system of two inclined tubes, where one functioned as an endoscope and the other exhibited sinusoidal wall deformation. Using the lubrication approach, the governing equations have been made simpler. Nadeem and Akbar[6] used the Adomian decomposition approach to investigate how heat transfer affected the peristaltic transport of a magnetohydrodynamic (MHD) Newtonian fluid with changing viscosity.

Extensive study has been conducted on pulsatile flows, which are significant in both biological and engineering contexts[7-10]. In their study on pulsatile MHD flow through two permeable beds, Malathy and Srinivas[7] presented analytical formulations for both the mass flux and the velocity profile. Based on their findings, velocity was suppressed as the intensity and frequency of the magnetic field increased. The pulsatile MHD Casson liquid flow under the

combined effects of radiation and chemical reaction was examined by Srinivas *et al*.[8]. Their results reveal that enhancing the Casson fluid and frequency parameters improves velocity. Additionally, the temperature increases as the heat source rises and decreases as the heat sink increases. Padma Devi and Srinivas[9] explored the combined effects of a porous medium and thermal radiation on the MHD pulsatile flow of two immiscible liquids. According to their research, a reduction in the thermal conductivity ratio enhances the temperature distribution. Komal and Srinivas[10] explored the combined effect of wall corrugations and channel curvature on the flow characteristics of a two-layered MHD flow of immiscible fluids in a corrugated curved channel under pulsatile pressure gradient.

A few studies indicated that in addition to the peristaltic flow driven by the vessel's wall motion, pulsatile flow effects must be included in the realistic model of blood flow in the smaller vessels[11-15]. Srivastava[11] investigated the effects of pulsatile flow on the peristaltic transport of a Newtonian viscous liquid within a flexible circular tube. Usha and Prema[12] have reported on the impact of peristaltic transport and pulsing flow caused by the fluid-particle suspension. Afifi and Gad[13] investigated how pulsatile and peristaltic liquid flow interact in a porous material. Gad[14] studied the peristaltic transport of a particle-liquid solution by examining the effects of periodic pressure gradient and Hall current. The heat transfer effects of pulsatile flow with peristalsis of particle fluid suspension have been investigated by Srinivas and Bala Anasuya[15]. Their findings show that temperature increases as wave number increases and decreases as particle concentration increases. Mekheimer[16] investigated MHD peristaltic transport in an inclined channel via perturbation expansion in δ. The analysis showed that magnetic field strength, Froude number, and inclination angle significantly alter the flow behaviour. Enhanced magnetic influence suppresses the central eddy and increases the overall pumping performance. Srinivas and Pushparaj[17] analyzed peristaltic flow in an inclined asymmetric channel, considering the effects of an applied magnetic field. They observed that inclination and magnetic effects significantly influence pressure rise and wall shear stress. Increasing the inclination amplifies the pressure gradient, while magnetic fields intensify wall stress. Ramesh and Devakar[18] reported peristaltic flow of a Casson liquid in an inclined channel, showing how channel inclination and plug width affect pressure rise, friction, and trapped bolus formation. Nagarani[19] investigated Casson fluid peristaltic transport in an inclined channel, revealing how inclination and yield stress control flow and bolus size.

Nanofluids are advanced heat transfer fluids formulated by dispersing nanosized particles into conventional base fluids, thereby enhancing their thermal properties. Common base fluids include water, blood, ethylene glycol, and kerosene, while nanoparticles such as oxides, nitrides, metalsand carbides are frequently employed. Compared to ordinary fluids, nanofluids exhibit higher viscosity and superior thermal conductivity. The incorporation of nanoparticles substantially improves heat and mass transfer characteristics, making nanofluids highly advantageous for various industrial applications, including electronic cooling, energy systems, chemical processing, and heat exchangers. Furthermore, their emerging use in biomedical applications, such as targeted drug delivery, cancer therapy, and diagnostics, demonstrates their potential to bridge technological innovations across both industrial and medical sectors. Choi and Eastman[20] introduced nanofluids by dispersing nanoparticles in base fluids, predicted significant thermal conductivity enhancement and highlighted their potential to improve heat transfer in practical applications. Extensive research on nanofluids has led to multiple studies[19-27] examining their thermal behaviour and properties. Abbasi *et al*.[21] analyzed the impact of velocity and thermal slip on mixed convective peristaltic transport of a copper-water nanofluid through an inclined channel. Their study revealed that nanoparticle concentration, slip effects, and channel inclination significantly affect the pressure gradient, velocity distribution, and heat transfer behaviour of the nanofluid. Vijayalakshmi and Srinivas[22] studied the effects of thermal radiation on hydromagnetic pulsatile flow of nanofluids in a porous channel. Their analysis, involving different nanoparticles, showed that thermal radiation, magnetic field, and porosity parameters significantly influence the velocity, temperature, and heat transfer characteristics of the flow. Ellahi *et al*.[23] analyzed the peristaltic transport of Ag-water and Cu-water nanofluids in a vertical asymmetric channel, incorporating entropy generation and the influence of a porous medium. They introduced a novel model for nanoparticle concentration and examined the flow characteristics and trapping phenomenon through analytical and

numerical approaches. Devaki *et al*.[24] examined the magnetohydrodynamic peristaltic flow of a copper-water nano fluid through a mildly stenosed artery, emphasizing the influence of nanoparticle shape. Their analysis indicates that nanoparticle geometry, size, and peristaltic amplitude significantly affect velocity, temperature, and pressure distribution, with brick-shaped particles enhancing temperature and bolus formation. Waqas *et al*.[25] explored the effect of shape factor on Sisko nanofluid flow with gold nanoparticles over a stretching surface. The study concluded that slip parameters decrease velocity and temperature profiles, whereas thermal radiation and nanoparticle volume fraction enhance thermal performance, linking particle geometry to heat transfer efficiency. In their study, Akbar *et al*.[26] analyzed the behaviour of shaped metallic nanoparticles in blood flow through diverging tapered stenosed arteries, emphasizing biomedical relevance. They found that flow velocity, shear stress, and bolus size vary notably with particle geometry and electromagnetic effects, where platelet-shaped nanoparticles demonstrated superior transport efficiency. Goyal and Srinivas[27] investigated how curvature and wall irregularities influence the pulsatile flow of a ternary hybrid nanofluid (Ag - MoS_2 - MWCNT) in a corrugated curved channel. Their findings indicate that the flow and heat-transfer behaviour are extremely sensitive to curvature, magnetic effects, and nanoparticle characteristics, providing valuable insights for biological and engineering transport applications. Rashid *et al*.[28] studied the lid-driven cavity flow of (Cu - Al_2O_3)/H_2O hybrid nanofluid, emphasizing the influence of nanoparticle geometry. Their study demonstrated that lamina-shaped nanoparticles yield the highest heat transfer, followed by column and spherical shapes.

Although several studies have addressed peristaltic and pulsatile flows, investigations that incorporate nanoparticle suspensions and channel inclination to evaluate heat transfer and flow behaviour are relatively scarce in the existing literature. The present work examines the transport properties of a blood, water and kerosene-based nanofluid in an inclined porous channel, where the influence of nanoparticle morphology (blade, lamina, columnar, and cylindrical) is explicitly considered. The flow is driven by the combined influence of peristaltic wall deformation and a pulsatile pressure gradient, with the governing equations solved using a small-amplitude perturbation technique. Extensive graphical results for velocity, temperature, streamlines, and isothermal contours are presented to demonstrate how inclination angle, nanoparticle concentration and particle shape affect the flow and heat-transfer behaviour.

Mathematical Formulation

Consider a two-dimensional channel of infinite length and mean width 2d. Fig. 1 illustrates that the flow is driven by a sinusoidal wave of small amplitude propagating along the flexible boundaries of the channel. The flow is considered to be an incompressible nanofluid suspension, consisting of a base fluid enriched with gold (Au) and silver (Ag) nanoparticles of different geometrical morphologies, including cylindrical, lamina, columnar, and blade-shaped configurations. The following is an expression for the governing equations that describe the momentum and temperature distributions of this nanofluid suspension[13-15].

$$\frac{\partial u}{\partial x}+\frac{\partial v}{\partial y}=0 \qquad \ldots(1)$$

$$\rho_{nf}\left[\frac{\partial u}{\partial t}+u\frac{\partial u}{\partial x}+v\frac{\partial u}{\partial y}\right]=-\frac{\partial p}{\partial x}+\mu_{nf}\left[\frac{\partial^2 u}{\partial x^2}+\frac{\partial^2 u}{\partial y^2}\right]-\frac{\mu_{nf}}{k}u+(\rho\beta)_{nf}g(T-T_0)sin\theta\ -\sigma_{nf}{B_0}^2u \qquad \ldots(2)$$

$$\rho_{nf}\left[\frac{\partial v}{\partial t}+u\frac{\partial v}{\partial x}+v\frac{\partial v}{\partial y}\right]=-\frac{\partial p}{\partial y}+\mu_{nf}\left[\frac{\partial^2 v}{\partial x^2}+\frac{\partial^2 v}{\partial y^2}\right]-\frac{\mu_{nf}}{k}v+(\rho\beta)_{nf}g(T-T_0)cos\theta \qquad \ldots(3)$$

$$(\rho C_p)_{nf}\left[\frac{\partial T}{\partial t}+u\frac{\partial T}{\partial x}+v\frac{\partial T}{\partial y}\right]=K_{nf}\left[\frac{\partial^2 T}{\partial x^2}+\frac{\partial^2 T}{\partial y^2}\right]-\frac{\partial q_r}{\partial y}+Q_0 \qquad \ldots(4)$$

The wall displacement of the channel is given by $\eta(x,t)\ = a\ cos\ (\frac{2\pi}{\lambda}(x-ct))$. Using the following dimensionless variables:

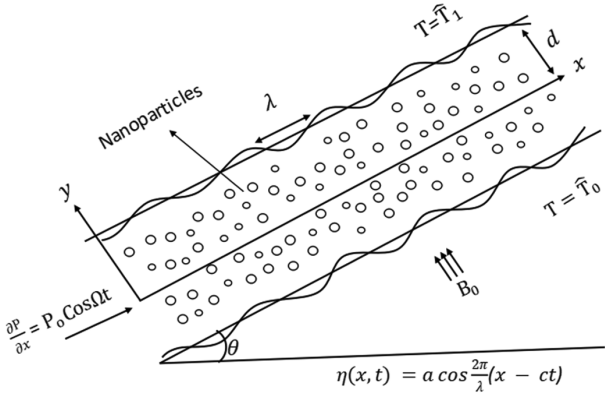

Fig. 1 — Schematic flow

$x^* = \frac{x}{d}$, $y^* = \frac{y}{d}$, $t^* = \frac{tc}{d}$, $p^* = \frac{p}{\rho c^2 d/\wedge}$, $k^* = \frac{k}{d^2}$, $u^* = \frac{u}{c}$, $v^* = \frac{v}{c}$, $T^* = \frac{T-T_0}{T_1-T_0}$,

The Reynolds number, wavenumber, Grashof number, and magnetic field parameter are given by

$$Re = \frac{cd}{\vartheta}, \alpha = \frac{2\pi d}{\lambda}, Gr = \frac{g\rho\beta(T-T_0)d^2}{c\mu} \; and \; M = \frac{\sigma B_0^2 d}{\rho c}$$

Introducing the nondimensional quantities and dropping the asterisks yield the reduced form of equations

$$\left[\frac{\partial u}{\partial t} + u\frac{\partial u}{\partial x} + v\frac{\partial u}{\partial y}\right] = -\frac{A_1}{2\pi}\frac{\partial p}{\partial x} + \frac{A_2}{Re}\left[\frac{\partial^2 u}{\partial x^2} + \frac{\partial^2 u}{\partial y^2}\right] - \frac{A_2}{Re\, k}u + \frac{A_3 G_r\, T\, sin\theta}{Re} - M\, A_4\, u \quad \ldots(5)$$

$$\left[\frac{\partial v}{\partial t} + u\frac{\partial v}{\partial x} + v\frac{\partial v}{\partial y}\right] = -\frac{A_1}{2\pi}\frac{\partial p}{\partial y} + \frac{A_2}{Re}\left[\frac{\partial^2 v}{\partial x^2} + \frac{\partial^2 v}{\partial y^2}\right] - \frac{A_2}{Re\, k}v + \frac{A_3 G_r\, T\, cos\theta}{Re} \quad \ldots(6)$$

$$\left[\frac{\partial T}{\partial t} + u\frac{\partial T}{\partial x} + v\frac{\partial T}{\partial y}\right] = \frac{A_5}{Re\, Pr}\left[\frac{\partial^2 T}{\partial x^2} + \frac{\partial^2 T}{\partial y^2}\right] + \frac{A_6\,\xi}{Re\, Pr} + \frac{4}{3}\frac{A_6\, Rd}{Re\, Pr} \quad \ldots(7)$$

The radiative heat flux is given by $q_r = -\frac{4\sigma^*}{3k^*}\frac{\partial T^4}{\partial y}$.where $\sigma^*$and $k^*$are the Stefan–Boltzmann constant and the mean absorption coefficient, and $T^4 \approx 4T_\infty^3 T - 3T_\infty^4$.

By taking $u = \frac{\partial \psi}{\partial y}$, $v = -\frac{\partial \psi}{\partial x}$ and on eliminating p in Eq. (5), (6) we get

$$Re\left[\frac{\partial^3\psi}{\partial y^2\partial t} + \frac{\partial\psi}{\partial y}\frac{\partial^3\psi}{\partial x\partial y^2} - \frac{\partial\psi}{\partial x}\frac{\partial^3\psi}{\partial y^3} + \frac{\partial^3\psi}{\partial x^2\partial y} + \frac{\partial\psi}{\partial y}\frac{\partial^3\psi}{\partial x^3} - \frac{\partial\psi}{\partial x}\frac{\partial^3\psi}{\partial x^2\partial y}\right] = A_2\left[\frac{\partial^4\psi}{\partial x^4} + \frac{\partial^4\psi}{\partial y^4} + 2\frac{\partial^4\psi}{\partial x^2\partial y^2}\right] - \frac{A_2}{k}\left[\frac{\partial^2\psi}{\partial x^2} + \frac{\partial^2\psi}{\partial y^2}\right] + A_3 G_r\,(sin\theta\frac{\partial T}{\partial y} + cos\theta\frac{\partial T}{\partial x}) - A_4 MRe\frac{\partial^2\psi}{\partial y^2} \quad ...(8)$$

$$RePr\left[\frac{\partial T}{\partial t} + \frac{\partial\psi}{\partial y}\frac{\partial T}{\partial x} - \frac{\partial\psi}{\partial x}\frac{\partial T}{\partial y}\right] = A_5\left[\frac{\partial^2 T}{\partial x^2} + \frac{\partial^2 T}{\partial y^2}\right] + \frac{4}{3}A_6 Rd\frac{\partial^2 T}{\partial y^2} + A_6(\xi) \quad \ldots(9)$$

Under the assumption of no horizontal wall displacement, $\eta(x,t)$ as the vertical displacement we have boundary conditions[11,12,15]

$$u = \psi_y = 0, y = \pm d \pm \eta$$

$$v = -\psi_x = \pm\frac{\partial\,\eta}{\partial t}$$

$$T = T_0 + \frac{a}{d}(T_1 - T_0)\cos\big(\alpha(x-t)\big)\; y = (d+\eta)$$

$$T = T_0 = -(d+\eta)$$

In the present analysis, the wave speed c of the imposed boundary wave and the imposed pressure gradient are considered equal, and an imposed pressure gradient is given by

$$\frac{\partial p}{\partial x} = p_0 cos\Omega t$$

where p_0 and Ω are arbitrary constants. The pressure gradient is assumed to be a function of the amplitude of wavemotion in the form of a perturbation series

$$\frac{\partial p}{\partial x} = \left(\frac{\partial p}{\partial x}\right)_0 + \epsilon\left(\frac{\partial p}{\partial x}\right)_1 + \epsilon^2\left(\frac{\partial p}{\partial x}\right)_2 + \cdots$$

where the first term represents the imposed periodic pressure gradient in dimensional form as

$\left(\frac{\partial p}{\partial x}\right)_0 = p_0 e^{At}$ where $A = \frac{\Omega d}{c}$

The parameter $A = \frac{\Omega d}{c}$ is identified as the reduced frequency, pertaining to the wave number of the oscillatory pressure gradient.

The amplitude ratio is assumed to be small, such that $\epsilon = \frac{a}{d} \ll 1$. In order to obtain the solution expanding the Eq. (8) – Eq. (9) in ψ, T as

$$\psi = \psi_0 + \epsilon\psi_1 + \epsilon^2\psi_2 + \cdots$$

$$T = T_0 + \epsilon T_1 + \epsilon^2 T_2 + \cdots$$

The process is similar to the C-S Yih[29], the zeroth and first order equations are given by

$$Re\left[\frac{\partial^3\psi_0}{\partial y^2\partial t} + \frac{\partial\psi_0}{\partial y}\frac{\partial^3\psi_0}{\partial x\partial y^2} - \frac{\partial\psi_0}{\partial x}\frac{\partial^3\psi_0}{\partial y^3} + \frac{\partial^3\psi_0}{\partial x^2\partial t} + \frac{\partial\psi_0}{\partial y}\frac{\partial^3\psi_0}{\partial x^3} - \frac{\partial\psi_0}{\partial x}\frac{\partial^3\psi_0}{\partial x^2\partial y}\right] = A_2\left[\frac{\partial^4\psi_0}{\partial x^4} + \frac{\partial^4\psi_0}{\partial y^4} + 2\frac{\partial^4\psi_0}{\partial x^2\partial y^2}\right] - \frac{A_2}{k}\left[\frac{\partial^2\psi_0}{\partial x^2} + \frac{\partial^2\psi_0}{\partial y^2}\right] + A_3 G_r\left(sin\theta\frac{\partial T_0}{\partial y} + cos\theta\frac{\partial T_0}{\partial x}\right) - A_4 Re\, M\frac{\partial^2\psi_0}{\partial y^2} \quad \ldots(10)$$

$$RePr\left[\frac{\partial T_0}{\partial t} + \frac{\partial\psi_0}{\partial y}\frac{\partial T_0}{\partial x} - \frac{\partial\psi_0}{\partial x}\frac{\partial T_0}{\partial y}\right] = A_5\left[\frac{\partial^2 T_0}{\partial x^2} + \frac{\partial^2 T_0}{\partial y^2}\right] + \frac{4}{3}A_6 Rd\frac{\partial^2 T_0}{\partial y^2} + A_6\,\xi \quad \ldots(11)$$

$$Re\left[\frac{\partial^3\psi_1}{\partial y^2\partial t} + \frac{\partial\psi_1}{\partial y}\frac{\partial^3\psi_0}{\partial x\partial y^2} + \frac{\partial\psi_0}{\partial y}\frac{\partial^3\psi_1}{\partial x\partial y^2} - \frac{\partial\psi_0}{\partial x}\frac{\partial^3\psi_1}{\partial y^3} - \frac{\partial\psi_1}{\partial x}\frac{\partial^3\psi_0}{\partial y^3} + \frac{\partial^3\psi_1}{\partial x^2\partial t} + \frac{\partial\psi_0}{\partial y}\frac{\partial^3\psi_1}{\partial x^3} + \frac{\partial\psi_1}{\partial y}\frac{\partial^3\psi_0}{\partial x^3} - \frac{\partial\psi_0}{\partial x}\frac{\partial^3\psi_1}{\partial x^2\partial y} - \frac{\partial\psi_1}{\partial x}\frac{\partial^3\psi_0}{\partial x^2\partial y}\right] = A_2\left[\frac{\partial^4\psi_1}{\partial x^4} + \frac{\partial^4\psi_1}{\partial y^4} + 2\frac{\partial^4\psi_1}{\partial x^2\partial y^2}\right] - \frac{A_2}{k}\left[\frac{\partial^2\psi_1}{\partial x^2} + \frac{\partial^2\psi_1}{\partial y^2}\right] +$$

$$\left(sin\theta\frac{\partial T_1}{\partial y}+cos\theta\frac{\partial T_1}{\partial x}\right)-A_4 Re\,M\frac{\partial^2\psi_1}{\partial y^2} \quad \ldots(12)$$

$$RePr\left[\frac{\partial T_1}{\partial t}+\frac{\partial\psi_0}{\partial y}\frac{\partial T_1}{\partial x}+\frac{\partial\psi_1}{\partial y}\frac{\partial T_0}{\partial x}-\frac{\partial\psi_0}{\partial x}\frac{\partial T_1}{\partial y}-\frac{\partial\psi_1}{\partial x}\frac{\partial T_0}{\partial y}\right]=$$
$$A_5\left[\frac{\partial^2 T_1}{\partial x^2}+\frac{\partial^2 T_1}{\partial y^2}\right]+\frac{4}{3}A_6 Rd\frac{\partial^2 T_1}{\partial y^2} \quad \ldots(13)$$

The conditions to solve the zeroth and first order equations are

$\psi_{0y}(\pm1)=0, \psi_{0x}(\pm1)=0,$
$\psi_{1y}(\pm1)\pm\psi_{0yy}(\pm1)\cos\alpha(x-t)=0,$
$\psi_{1x}(\pm1)\pm\psi_{0xy}(\pm1)\cos\alpha(x-t)$
$=\mp\beta\sin\alpha(x-t),$
$T_0(\pm1)=0, \quad T_1(1)=0, T_1(1)=\cos\alpha(x-t)$

The zeroth order solution represents an oscillating flow between infinite walls whose solution is given by

$$u_0(y,t)=\frac{\partial\psi_0}{\partial y}=if_0(y)e^{iAt}, T_0(y,t)=ig_0(y)e^{iAt}$$

Where

$f_0(y)=\frac{L_6\cos h(L_3 y)}{\cos h L_3}+\frac{A_1 Re}{A_2 {L_3}^2}-L_4\left(\frac{\cos h(L_1)}{{L_1}^2-{L_3}^2}-\frac{1}{{L_3}^2}\right);$
$g_0(y)=\frac{A_6\xi}{{L_1}^2}\left[1-\frac{\cos h(L_1 y)}{\cos h L_1}\right];$
$\psi_1(x,y,t)=\sum_{-\infty}^{\infty}\psi_{1,n}e^{inax}$;
$T_1(x,y,t)=\sum_{-\infty}^{\infty}T_{1,n}e^{inax}$

Here, ψ_1 and T_1 are functions of *x*, *y*, and *t*, while $\psi\ (1,n)$ and $T\ (1,n)$ depend only on *y* and *t*. The integer *n* ranges from $-\infty$ to ∞, with negative indices indicating complex conjugates. Non-trivial solutions exist solely for $n=\pm1$. Under the long-wave assumption ($\alpha\ll1$), the above equations are expanded in powers of α following C-S Yih[29].

$\psi_{1,1}=e^{\mu t}\chi_1(y,t)$
$T_{1,1}=e^{\mu t}\tau_1(y,t)$
$\chi_1(y,t)=\phi_0(y,t)+\alpha\phi_1(y,t)+O(\alpha^2)$
$\tau_1(y,t)=\theta_0(y,t)+\alpha\theta_1(y,t)+$

$$A_2\frac{\partial^4\phi_0}{\partial y^4}+\left(\frac{A_2}{K}-A_4 M\,Re\right)\frac{\partial^2\phi_0}{\partial y^2}-Re\frac{\partial}{\partial t}\frac{\partial^2\phi_0}{\partial y^2}+$$
$$A_3 Gr\left(\frac{\partial\theta_0}{\partial t}\sin\theta+\theta_0\, i\alpha\cos\theta\right)=0 \quad \ldots(14)$$

$$\frac{\partial^2\theta_0}{\partial y^2}\left(A_5+A_6\frac{4}{3}Rd\right)-RePr\frac{\partial\theta_0}{\partial t}=0 \quad \ldots(15)$$

$$A_2\frac{\partial^4\phi_1}{\partial y^4}+\left(\frac{A_2}{K}-A_4 M\,Re\right)\frac{\partial^2\phi_1}{\partial y^2}-Re\left(\frac{\partial}{\partial t}\frac{\partial^2\phi_1}{\partial y^2}+\right.$$
$$\left.i\frac{\partial^2\phi_0}{\partial y^2}f_0 e^{iAt}-i\phi_0 {f_0}'' e^{iAt}\right)+A_3 Gr\left(\frac{\partial\theta_1}{\partial t}\sin\theta+\right.$$
$$\left.\theta_1\, i\alpha\cos\theta\right)=0 \quad \ldots(16)$$

$$\frac{\partial^2\theta_1}{\partial y^2}\left(A_5+A_6\frac{4}{3}Rd\right)-RePr\frac{\partial\theta_1}{\partial t}=0 \quad \ldots(17)$$

With the boundary conditions are

$\phi_0(\pm1)=\pm e^{-i\alpha t}, \theta_0(-1)=\theta_0(1)=e^{-i\alpha t}$
$\phi_0'(\pm1)=\mp\frac{i}{2}f_0'(\pm)e^{-i\omega_2 t}-{f_0}^{*'}(\pm)e^{-i\omega_1 t}$
$\phi_0(\pm1,t)=0, \quad \phi_1'(\pm1,t)=0$
$\theta_1(\pm1,t)=0$

Solution for the Eq. (14) and (15)

$$\phi_0(y,t)=s_1(y)e^{-i\alpha t}+s_2(y)e^{i\omega_2 t}+s_3(y)e^{-i\omega_1 t} \quad \ldots(18)$$

$$\theta_0(y,t)=r_1(y)e^{-i\alpha t}+r_2(y)e^{i\omega_2 t}+r_3(y)e^{-i\omega_1 t} \quad \ldots(19)$$

Where

$$s_1(y)=y-\frac{\sinh L_1 y-y\sinh L_1}{L_1\cosh L_1-\sinh L_1} \quad \ldots(20)$$

$$s_2(y)=\frac{-\frac{i}{2}f_0'(1)(\sinh L_2 y-y\sinh L_2)}{L_2\cosh L_2-\sinh L_2} \quad \ldots(21)$$

$$s_2(y)=\frac{\frac{i}{2}{f*_0}'(1)(\sinh L_3 y-y\sinh L_3)}{L_3\cosh L_3-\sinh L_3} \quad \ldots(22)$$

$$r_1=\frac{A_6*\xi}{{L_1}^2}\left[1-\frac{\cosh L_1 y}{\cosh L_1}\right]$$

$\omega_1=A+\alpha, \omega_2=A-\alpha$

The conditions $f_0'(1)=-f_0'(-1)$ and ${f_0}^{*'}(1)=-{f_0}^{*'}(-1)$ have been applied to simplify the resulting Expressions[13]. The solution of Eqs (20-22), though conceptually straightforward, is extensive due to the presence of non-homogeneous terms. It comprises multiple harmonic contributions of the form $e^{-i\alpha t}, e^{i\omega_2 t}$ and $e^{-i\omega_1 t}$ which originate from the convective acceleration terms. These terms represent the interaction between the periodic wall induced flow and the externally imposed periodic pressure. Notably, this interaction generates an intriguing first-order steady flow component in both the ϕ_1 and θ_1 contributions.

Steady flow

If we allow $A\to\alpha$, the resulting flow contains a time-independent component in addition to the periodic components. The first-order solution is tedious to obtain. In order to examine the interaction of pulsatile and peristaltic flow, we consider the steady-state condition by extracting the time-

independent component from the periodic terms. The steady components are represented as

$$\phi s = \phi 0 + \alpha\phi 1 + .. \quad ...(23)$$

$$\theta s = \theta 0 + \alpha\theta 1 + .. \quad ...(24)$$

where the solution for the ϕ_0 and θ_0 are taken from the first term of the Eqn. (18) and (19) and ϕ_1 and θ_1 are given by

$$A_2 \frac{\partial^4 \phi_1}{\partial y^4} + \left(\frac{A_2}{K} - A_4 M\, Re\right)\frac{\partial^2 \phi_1}{\partial y^2} - Re\left(f_0 p_1 - f_0'' p_1\right) + A_3\, Gr(\theta_1\, i\alpha\cos\theta) = 0 \quad ...(25)$$

$$\frac{\partial^2 \theta_1}{\partial y^2}\left(A_5 + A_6\, \frac{4}{3} Rd\right) = RePr[f_0 b_1 - g_0' p_1] \quad ...(26)$$

with the boundary condition

$$\phi_1(\pm 1) = 0, \phi_1'(\pm 1) = 0\ and \theta_1(\pm 1) = 0$$

The solutions are given by

$$\phi_1(y) = c_1 + c_2 y + c_3\cosh(\lambda y) + c_3\sinh(\lambda y) + F_1(y) + F_2(y) + F_3(y) \quad ...(27)$$

$$\theta_1(y) = D\, Re\, \Pr\left[\frac{L_3^2\cosh(L_3 y) b_1}{L_6}\cosh(L_3 y) + 2A_2 L_3^2 b_1 A_1 Re y^2 - \frac{L_1^2\cosh(L_1 y) b_1}{L_4\cosh(L_1)} - 2L_3^2 b_1 y^2\right] + DL_1^2\cosh(L_1)\, RePr p_1 A_6\, \xi\cosh(L_1 y) + c_3 + c_4 y \quad ...(28)$$

Where

$$A_1 = \frac{1}{(1-\varphi_1) + \frac{\varphi_1\rho_1}{\rho_f}},\ A_2 = \frac{1}{(1-\varphi_1)^{2.5} + \left[(1-\varphi_1) + \frac{\varphi_1\rho_1}{\rho_f}\right]},$$

$$A_3 = \frac{(1-\varphi_1) + \frac{\varphi_1\rho_1\beta_1}{\rho_f\beta_f}}{(1-\varphi_1) + \frac{\varphi_1\rho_1}{\rho_f}}$$

$$A_4\frac{\frac{\sigma_1 + (n-1)\rho_f - (n-1)\varphi_1(\sigma_f - \sigma_1)}{\sigma_1 + (n-1)\rho_f + \varphi_1(\sigma_f - \sigma_1)}}{(1-\varphi_1) + \frac{\varphi_1\rho_1}{\rho_f}},\ A_5 = \frac{\frac{K_1 + (n-1)K_f - (n-1)\varphi_1(K_f - K_1)}{K_1 + (n-1)K_f + \varphi_1(K_1 - K_f)}}{(1-\varphi_1) + \frac{\varphi_1\rho_1 c_{p1}}{\rho_f c_{pf}}},\ A_6 = \frac{1}{(1-\varphi_1) + \frac{\varphi_1\rho_1 c_{p1}}{\rho_f c_{pf}}},$$

$$L_1 = \sqrt{\frac{Re\,\Pr\, i\, A}{A_5 + \frac{4}{3}Rd\, A_6}},\ L_3 = \sqrt{\frac{i\, A\, Re}{A_2} + \frac{1}{k} + \frac{A_4\, M\, Re}{A_2}},\ L_4 = \frac{A_3 A_6\, Gr\, sin\theta\, \xi}{A_2 L1^2},$$

$$L_6 = L_4\left[\frac{cosh\, L1}{L1^2 - L3^2} - \frac{1}{L3^2}\right] - \frac{A_1\, Re}{A_2 L3^2},\ L_8 = \sqrt{\frac{A_4\, M\, Re}{A_2} - \frac{1}{k}},$$

$$L_9 = -\frac{A_3\, Gr\, I\, \alpha\, cos\theta}{A_2},$$

$$L_{10} = \sqrt{\frac{L8^2 + \sqrt{L8^4 + 4L9}}{2}},\ L_{11} = \sqrt{\frac{L8^2 - \sqrt{L8^4 + 4L9}}{2}},\ L_{12} = A_5 + A_6\, Rd,$$

$$s_1 = -A_6 D L_1^2\phi_0 PrRe\beta\cosh[L_1^2] + \frac{D\, Re\,\Pr(L_1^2 L_6\cosh[L_1^2] - L_3^2 L_4(L_6(-3+2A_1A_2\, Re) + \cosh[L_3^2]))\phi_0}{L_4 L_6},$$

$$s_2 = \frac{1}{\sinh[\lambda]},\ s_3 = \frac{-1}{\sinh[\lambda]},\ s_4 = \frac{\cosh[\lambda]}{\sinh[\lambda]},\ s_5 = (F_1 + F_2 + F_3)\frac{1}{\sinh[\lambda]},$$

$$s_6 = -\frac{(1 + s_2\sinh[\lambda])}{\cosh[\lambda] + s_4\sinh[\lambda]},\ s_7 = -\frac{(1 + s_3\sinh[\lambda])}{\cosh[\lambda] + s_4\sinh[\lambda]},\ s_8 = -\frac{F_1 + F_2 + F_3 + s_5\sinh[\lambda]}{\cosh[\lambda] + s_4\sinh[\lambda]},$$

$$s_9 = -\frac{(s_2 + s_4 s_6)\lambda\cosh[\lambda] - s_6\lambda\sinh[\lambda]}{1 + (s_3 + s_4 s_7)\lambda\cosh[\lambda] - s_7\lambda\sinh[\lambda]},$$

$$s_{10} = -\frac{s_5\sinh[\lambda] + s_4 s_8\lambda\cosh[\lambda] - s_8\lambda\sinh[\lambda]\, F_1 + F_2 + F_3 + s_5\sinh[\lambda]}{1 + (s_3 + s_4 s_7)\lambda\cosh[\lambda] - s_7\lambda\sinh[\lambda]},$$

$$F_1 = \left(\frac{A}{2}\right) Re\, p1\left(\frac{(L_3^4 - \lambda^2 L_3^2)cosh[L_3]}{L_3^6}\right)\cosh[L_3\, y] + \left(\frac{(L_3^4 - \lambda^2 L_3^2)sinh[L_3])}{L_3^7}\right)\sinh[L_3\lambda] - ((L_1^4 - \lambda^2 L_1^2)\cosh[L_1\, y])/ L_1^4\cosh[L_1]\cosh[L_1 y])),$$

$$F_2 = \left(\frac{A}{2}\right) Re\, p1\left(\frac{(L_3^4 - \lambda^2 L_3^2)cosh[L_3]}{L_3^6 L_3^2}\right)\cosh[L_3\, y] + \left(\frac{(L_3^4 - \lambda^2 L_3^2)sinh[L_3])}{L_3^7 L_3^2}\right)\sinh[L_3\lambda] - ((L_1^4 - \lambda^2 L_1^2)\cosh[L_1\, y])/ L_1^4 L_3^2\cosh[L_1]\cosh[L_1 y])),$$

$$F_3 = \left(\frac{A}{2}\right) A_3 Gr\, i\, \alpha\cos[\theta]\ (D\, Re\,\Pr\, b_1(L_3^2\left(\frac{(L_3^4 - \lambda^2 L_3^2)\cosh[L_3]}{L_3^6}\right)\cosh[L_3\, y] + (L_3^2\left(\frac{(L_3^4 - \lambda^2 L_3^2)\sinh[L_3]}{L_3^7 L_3^2}\right)\sinh[L_3\, y] - \left(\frac{(L_1^4 - \lambda^2 L_1^2)\cosh[L_1 y]}{L_1^4 L_1^2\cosh[L_1]}\right),$$

Results and Discussion

The expression for thermophysical properties and the values for blood, water, kerosene, and nanoparticles and the shape factor values for the different nanoparticle shapes are given in Tables S1-S3 in Supplementary Information. The velocity profile is illustrated in Figs 2-4. By considering that $u_1 = \phi_1'$ and for $\frac{P_0}{2\pi} = -1$, a graphic interpretation for $\phi_1'\ and\ \theta_1$ has been shown. The fluid velocity falls as the value of *M* rises, as shown in Fig. 2(a). The suppression in velocity distribution is physically explained by the Lorentz force, a magnetic-field-induced drag that resists the fluid motion, leading to a significant deceleration of the flow. A highly porous media is indicated by small values of *k*, whereas the absence of a porous medium is represented by the limiting case ($k \to \infty$). Especially, flow is more difficult in a highly porous material. Fig. 2(b) illustrates how

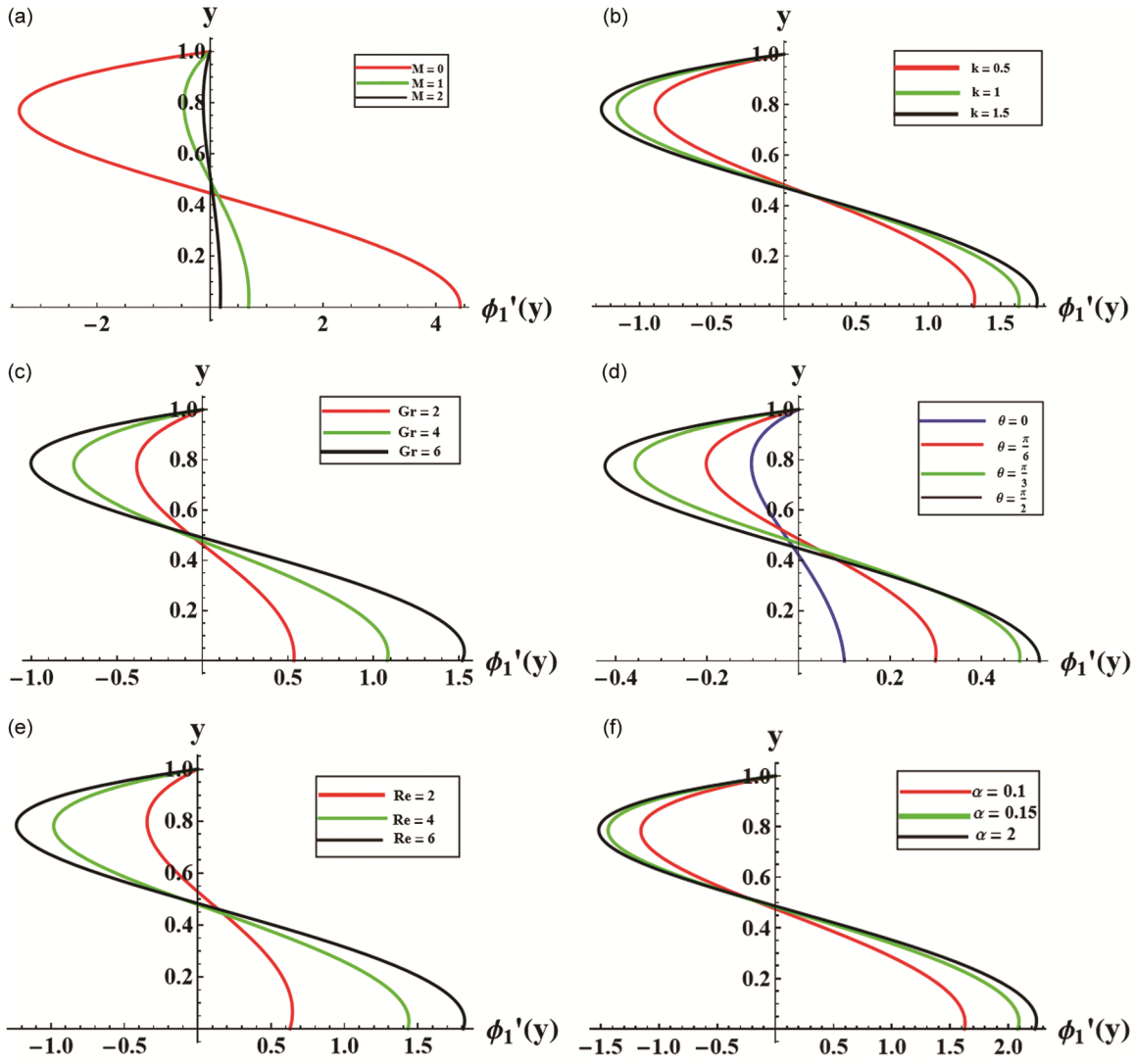

Fig. 2 — Velocity distribution for (a) different Hartmann numbers with fixed parameters $k = 1$, $Gr = 5$, $\theta = \pi/4$, $Re = 5$, $\alpha = 0.1$. (b) different permeability parameters with fixed $M = 1$, $Gr = 5$, $\theta = \pi/4$, $Re = 5$, $\alpha = 0.1$. (c) different Grashof numbers with fixed $k = 1$, $M = 1$, $\theta = \pi/4$, $Re = 5$, $\alpha = 0.1$. (d) different inclination angles with fixed $k = 1$, $Gr = 5$, $M = 1$, $Re = 5$, $\alpha = 0.1$. (e) different Reynolds numbers with fixed $k = 1$, $Gr = 5$, $\theta = \pi/4$, $M = 1$, $\alpha = 0.1$. (f) different wavenumbers with fixed $k = 1$, $Gr = 5$, $\theta = \pi/4$, $Re = 5$, $M = 1$

the axial velocity escalates as k rises. Fig. 2(c) illustrates how the velocity dispersion grows as the Grash of number rises. As seen in Fig. 2(c), a rise in Gr physically denotes the strength of the flow, a reduction in the viscous effects and an increase in velocity. The velocity profiles for various inclination angles (θ) are displayed in Fig. 2(d). Because the gravitational force is stronger at higher inclinations, velocity is increased. Fig. 2(e) demonstrates that when the Reynolds number rises, the viscosity decreases and the fluid's velocity increases. The velocity of the fluid increases with wavenumber α, as seen in Fig. 2(f).

Fig. 3(a-c) illustrates the velocity profiles of Au and Ag nanoparticle-using three different base fluids-water, kerosene, and blood under identical flow conditions ($Re = 25, M = 1, Gr = 5, k = 1, \alpha = 0.1, \theta = \pi/4$). The figure clearly indicates that both the type of nanoparticle and the base fluid significantly influence the fluid velocity within the channel. When comparing the base fluids, the velocity is found to be highest for the water-based nanofluid, followed by the kerosene-based nanofluid, and lowest for the blood-based nanofluid.

This order is mainly attributed to the variation in the thermophysical properties of the fluids. Water, having relatively low viscosity and good thermal conductivity, allows faster flow. Kerosene, being more viscous, offers moderate resistance, while blood

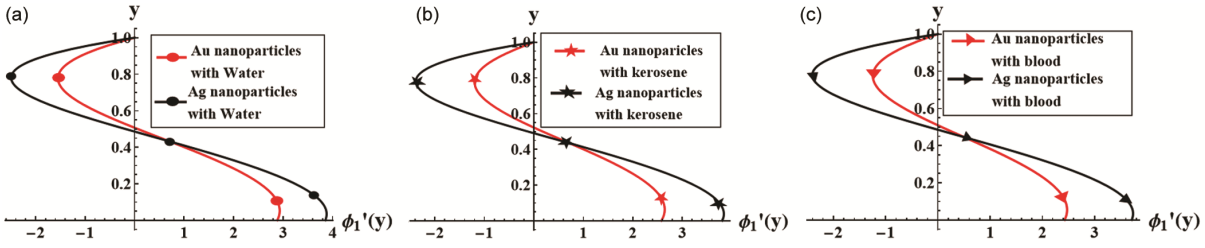

Fig. 3 — Comparison for Au and Ag nanoparticles: (a) Water-based nanofluid for $Re = 25$, $M = 1$, $Gr = 5$, $k = 1$, $\alpha = 0.1$, and $\theta = \pi/4$; (b) Kerosene-based nanofluid for $Re = 25$, $M = 1$, $Gr = 5$, $k = 1$, $\alpha = 0.1$, and $\theta = \pi/4$,; (c) Blood-based nanofluid for $Re = 25$, $M = 1$, $Gr = 5$, $k = 1$, $\alpha = 0.1$, and $\theta = \pi/4$

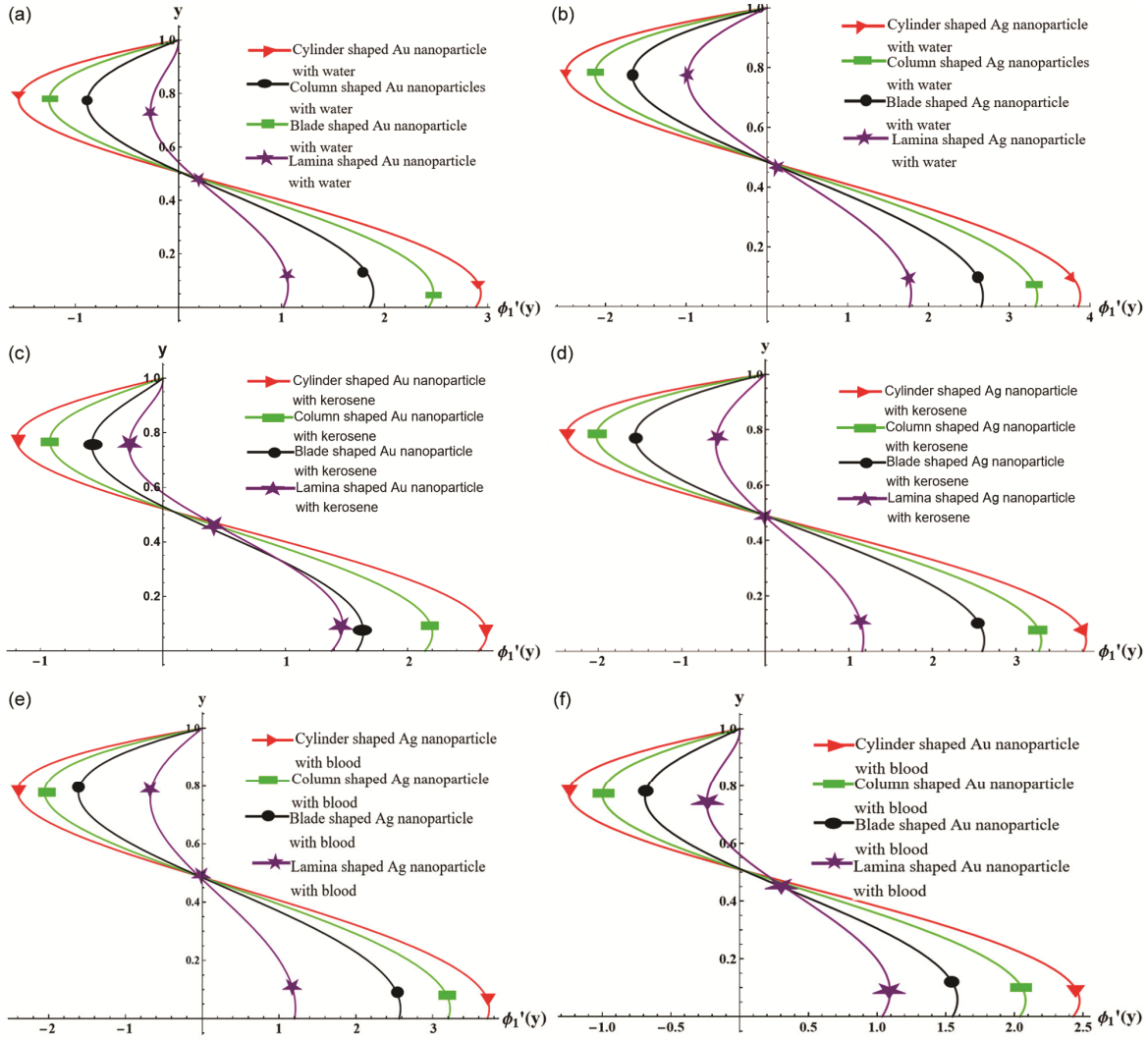

Fig. 4 — Illustration of differently shaped nanoparticles dispersed in various base fluids: (a, b) Au and Ag nanoparticles in water; (c, d) Au and Ag nanoparticles in kerosene; (e, f) Au and Ag nanoparticles in blood

with comparatively higher viscosity and complex rheological behaviour shows the least velocity. These observations confirm that both nanoparticle geometry and base fluid properties have a strong influence on the velocity field.

Fig. 4(a - f) depicts the velocity distribution for various nanoparticle shapes (cylindrical, column, blade and lamina) dispersed in different base fluids - water, kerosene, and blood using Au and Ag nanoparticles. In all cases, the velocity attains its

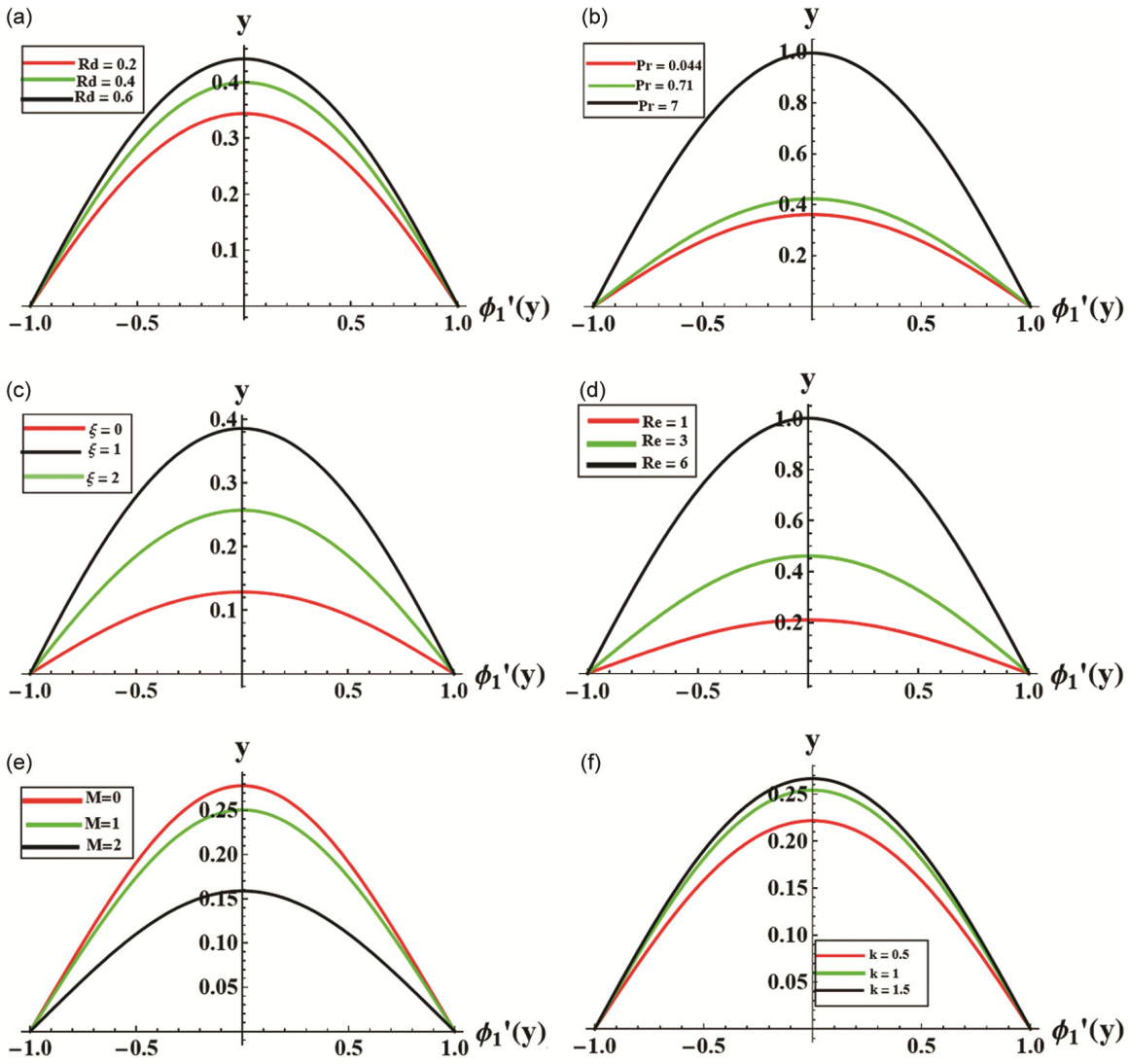

Fig. 5 — Temperature distributions for different parameters: (a) varying *Rd* (*P r* = 1, $\xi = -2$, *Re* = 1, *M* = 1, *k* = 1); (b) varying Prandtl number (*Rd* = 0.5, $\xi = -2$, *Re* = 1, *M* = 1, *k* = 1); (c) varying ξ (*P r* = 1, *Rd* = 0.5, *Re* = 1, *M* = 1, *k* = 1); (d) varying Reynolds number (*P r* = 1, $\xi = -2$, *Rd* = 0.5, *M* = 1, *k* = 1); (e) varying Hartmann number (*P r* = 1, $\xi = -2$, *Re* = 1, *Rd* = 0.5, *k* = 1); (f) varying permeability parameter (*P r* = 1, $\xi = -2$, *Re* = 1, *M* = 1, *Rd* = 0.5)

maximum for cylindrical shaped nanoparticles and its minimum for lamina shaped ones, indicating that the cylindrical geometry enhances fluid motion because of greater effective surface interaction. Fig. 5(a) illustrates the impact of *Rd*. The temperature profile enhances as *Rd* rises. As shown in Fig. 5(b), the liquid temperature rises as *Pr* increases (i.e., *Pr* = 0.044, 0.71 and 7 which correspond to mercury, air and water, respectively). Fig. 5(c) shows that the temperature increases as ξ rises. In this case, heat generation is represented by $\xi > 0$ and heat absorption by $\xi < 0$. As thermal energy is released inside the system, heat production occurs, raising the temperature of the flow field. As seen in Fig. 5(d), 5(e), and 5(f), the temperature distribution escalates as Reynolds number and permeability parameter rises while falling as Hartman number increases.

The trapping phenomenon, which occurs when a bolus of fluid is encircled by circulating streamlines, is a notable mechanism linked to peristalsis. The trapped bolus travels ahead due to the sinusoidal propagation of the peristaltic wave. This trapping process is important in physiological circumstances, including the movement of food boluses in the gastrointestinal system and blood flow linked to thrombus development. In Fig. 6 and Fig. 7, the

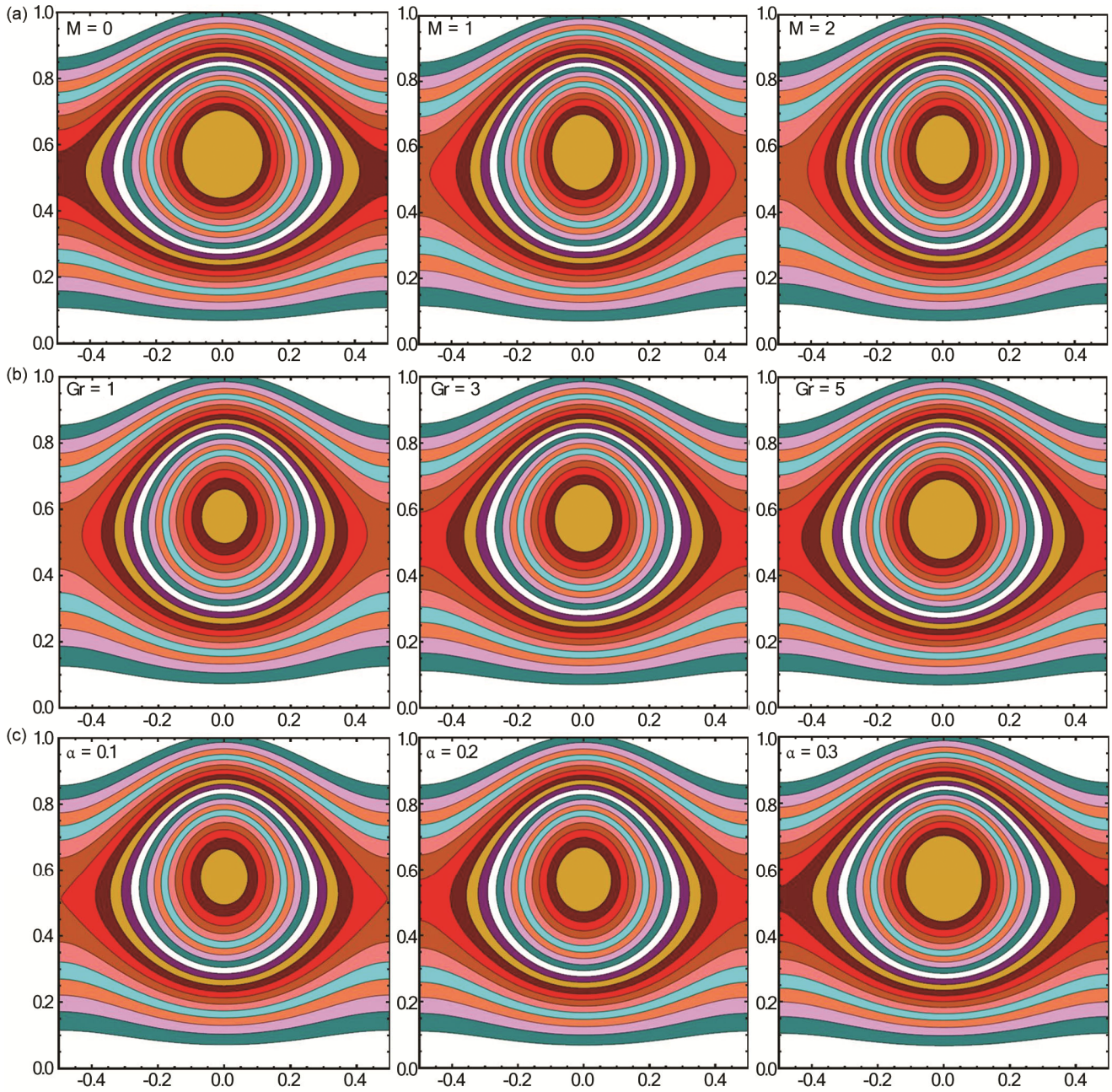

Fig. 6 — Streamlines in the wave frame: (a) Various values of M with fixed $\alpha = 0.1$, $Gr = 5$, $k = 1$, $Re = 5$; (b) Various values of Gr with fixed $\alpha = 0.1$, $M = 1$, $k = 1$, $Re = 5$. (c) Various values of α with fixed $M = 1$, $Gr = 5$, $k = 1$, $Re = 5$.

streamline patterns are discussed by adjusting parameters such as *M, Gr, α, k, Re*. The effect of varying the magnetic field strength on the formation of the bolus is illustrated in Fig. 6(a). It is observed that as the Hartmann number rises, the bolus size reduces. This reduction occurs because the Lorentz body force becomes more dominant over the viscous hydrodynamic forces at higher Hartmann numbers, thereby suppressing the bolus formation. As shown in Fig. 6(b), higher values of the Grashof number intensify the bolus formation, resulting in an enlarged trapping region. As demonstrated in Fig. 6(c), enhancement in the pressure gradient wavenumber contributes to a significant growth in the bolus size.

Fig. 7(a) shows that higher permeability of the porous space enhances the fluid flow, resulting in larger bolus formation as k rises. Fig. 7(b) indicates that higher Reynolds numbers escalate the fluid

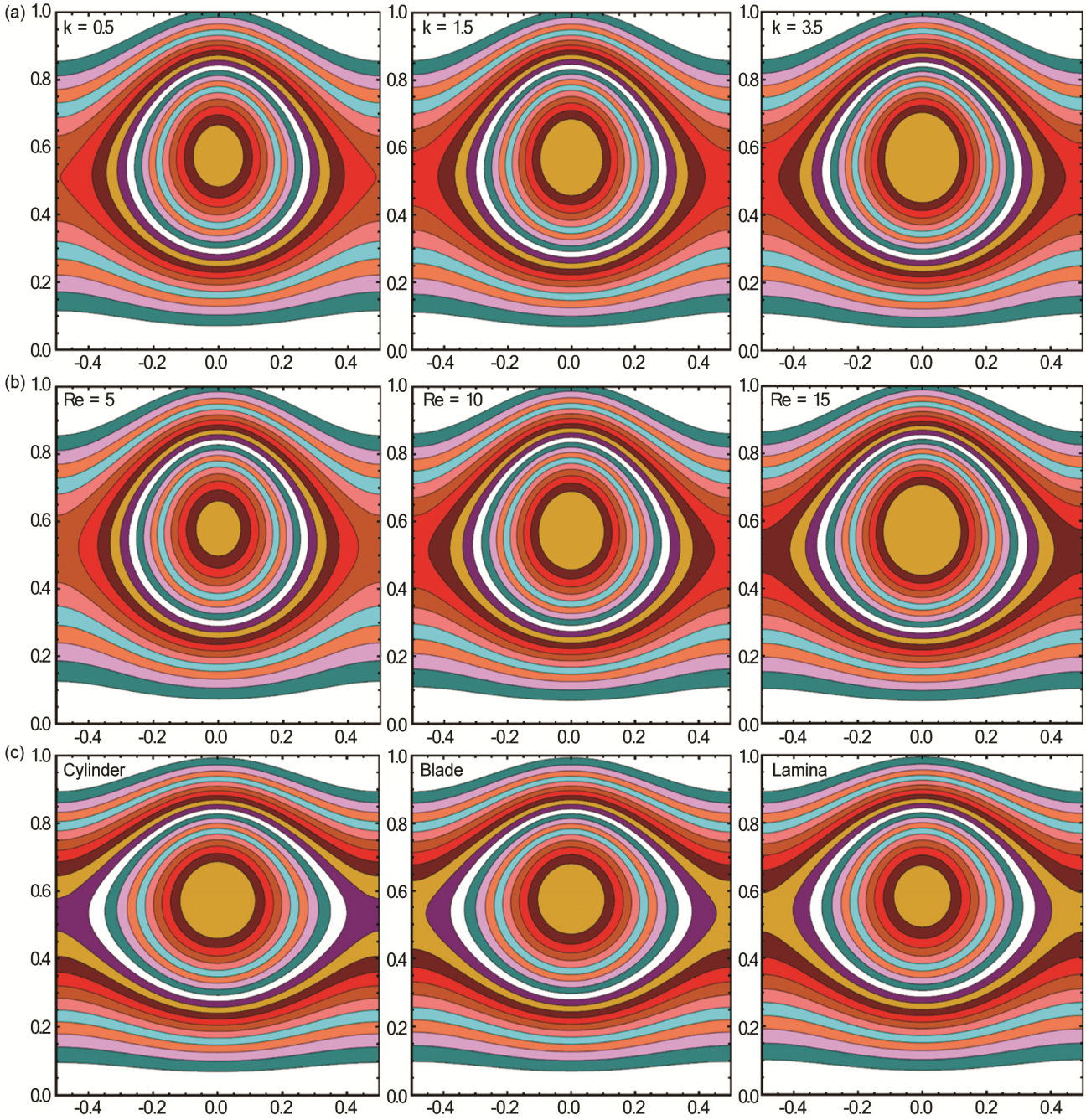

Fig. 7 — Streamlines in the wave frame: (a) Various values of k with fixed $\alpha = 0.1$, $Gr = 5$, $M = 1$, $Re = 5$; (b) Various values of Re with fixed $\alpha = 0.1$, $Gr = 5$, $k = 1$, $M = 1$. (c) Streamlines for shapes: Cylinder, Blade and Lamina for $\alpha = 0.1$, $Gr = 5$, $k = 1$, $M = 1$ $Re = 5$

velocity, thereby enlarging the trapped bolus region. Fig. 7(c) illustrates the streamline patterns for various nanoparticle shapes, showing a reduction in the number of boluses. Among these geometries, cylinder-shaped nanoparticles form the largest bolus, blade-shaped particles produce a moderately sized bolus, while lamina-shaped nanoparticles result in the smallest bolus.

Fig. 8 and Fig. 9 present the isothermal contour plots illustrating the temperature distribution of the nanofluid under the influence of various physical parameters. In Fig. 8(a), increasing the thermal radiation parameter (Rd) raises the nanofluid temperature, indicating enhanced thermal energy absorption. As shown in Fig. 8(b), higher Hartmann numbers (M) reduce the temperature, as the magnetic

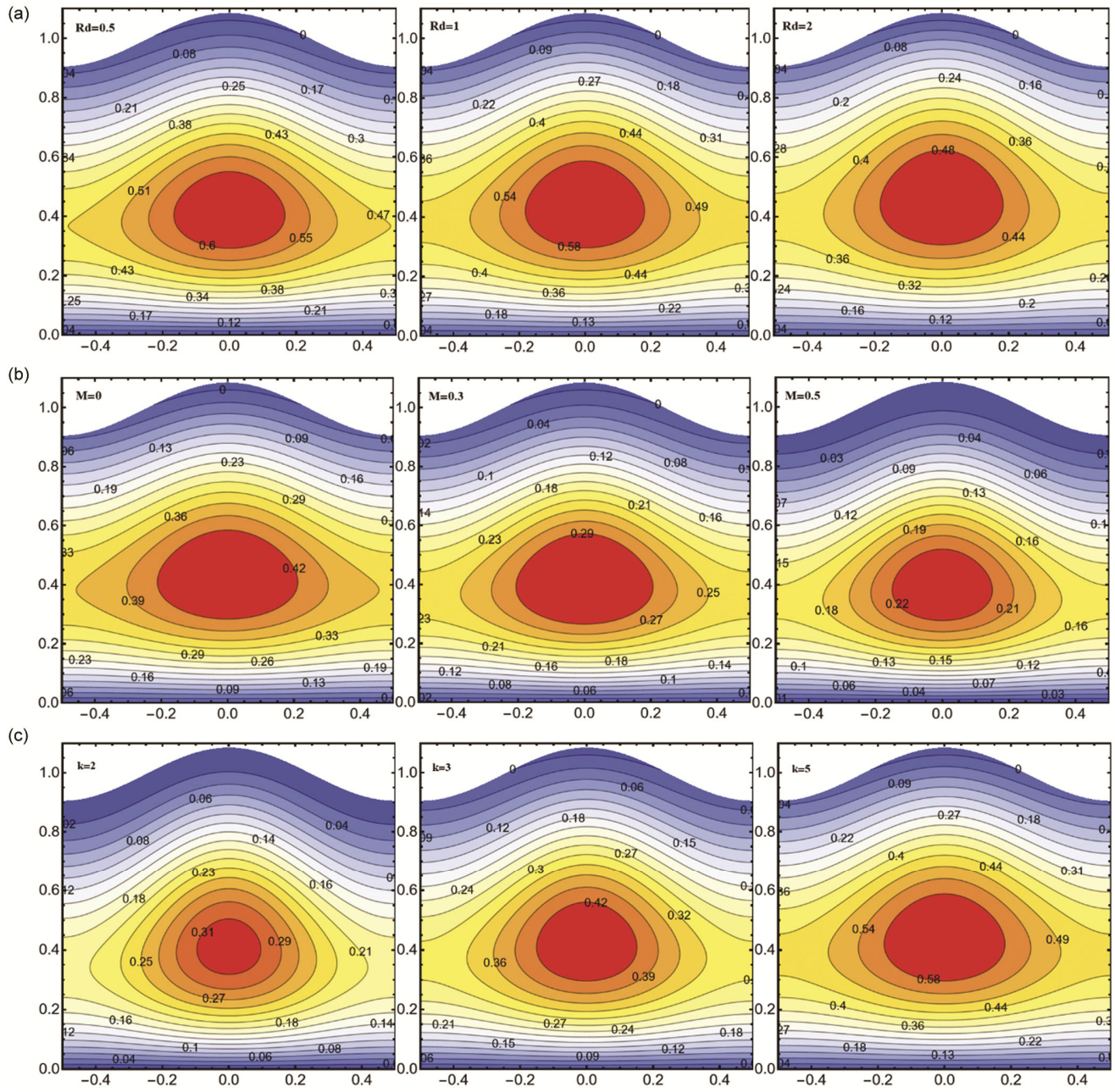

Fig. 8 — Isothermal lines: (a) For various values of *Rd* with fixed *Re* = 5, *P r* = 7, *M* = 1, *k* = 1; (b) For various values of *M* with fixed *Rd* = 0.5, *P r* = 7, *Re* = 5, *k* = 1; (c) For various values of *k* with fixed *Rd* = 0.5, *P r* = 7, *M* = 1, *Re* = 5

field suppresses fluid motion and promotes heat dissipation. The effect of the porous parameter (k) is depicted in Fig. 8(c), where increase in k leads to higher temperatures due to greater fluid penetration and heat accumulation within the porous medium.

Fig. 9(a) shows that increasing the Prandtl number (Pr = 0.044, 0.71, 7 for mercury, air, and water) elevates temperature, as thermal diffusion dominates over momentum transport. Fig. 9(b) demonstrates that higher Reynolds numbers (Re) promote stronger convective heat transfer, which leads to an elevated nanofluid temperature. As shown in Fig. 9(c), the shape of nanoparticles significantly influences the thermal behaviour. Cylinder-shaped nanoparticles display relatively lower temperatures within the isothermal contours, whereas lamina-shaped nanoparticles exhibit higher temperatures, demonstrating their greater thermal enhancement capability.

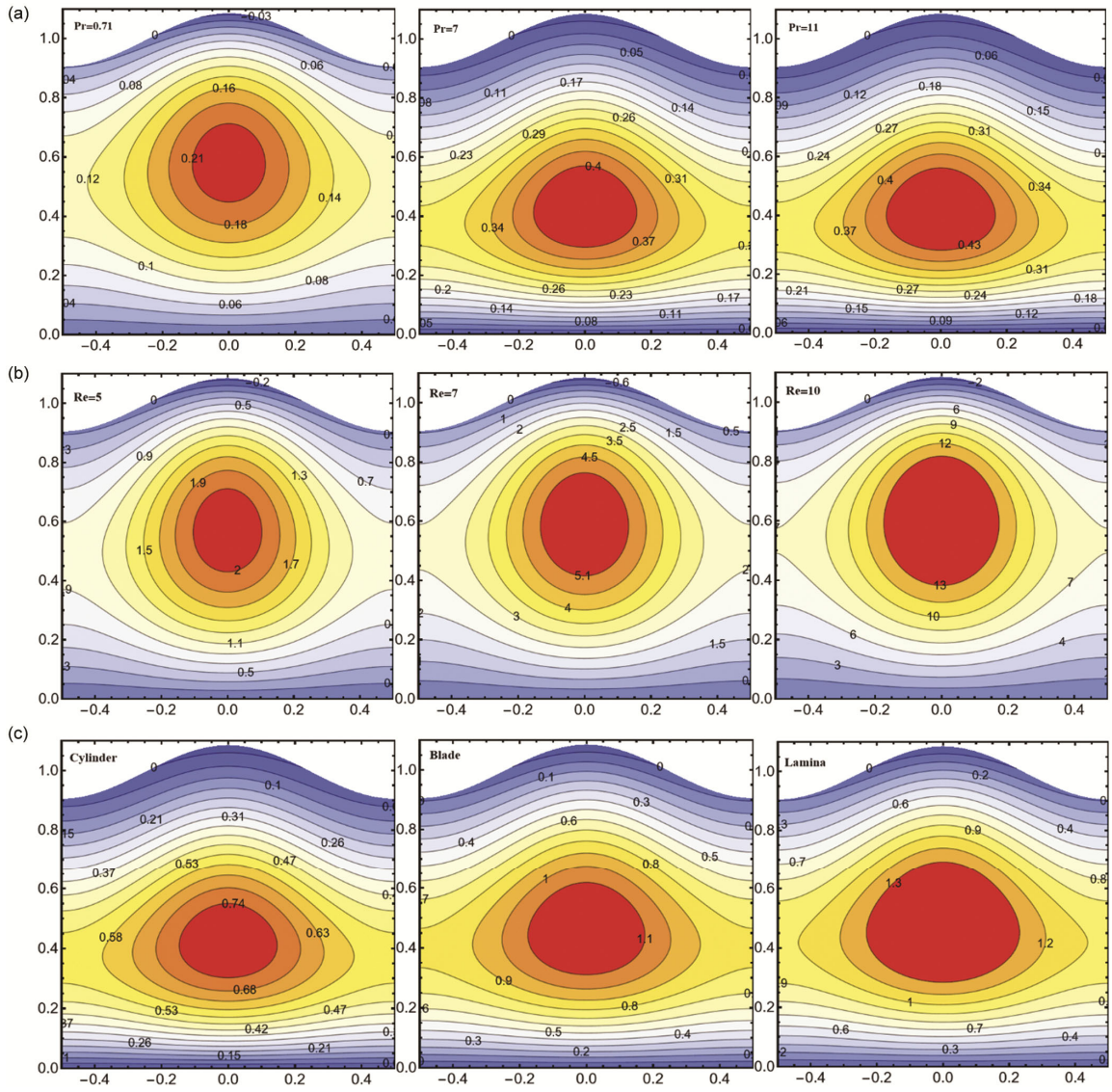

Fig. 9 — Isothermal lines: (a) For various values of $P\,r$ with fixed Rd = 0.5, Re = 5, M = 1, k = 1; (b) For various values of Re with fixed Rd = 0.5, $P\,r$ = 7, M = 1, k = 1; (c) isothermal lines for shapes: Cylinder, Blade and Lamina for Rd = 0.5, $P\,r$ == 7, k = 1, M = 1 Re = 5

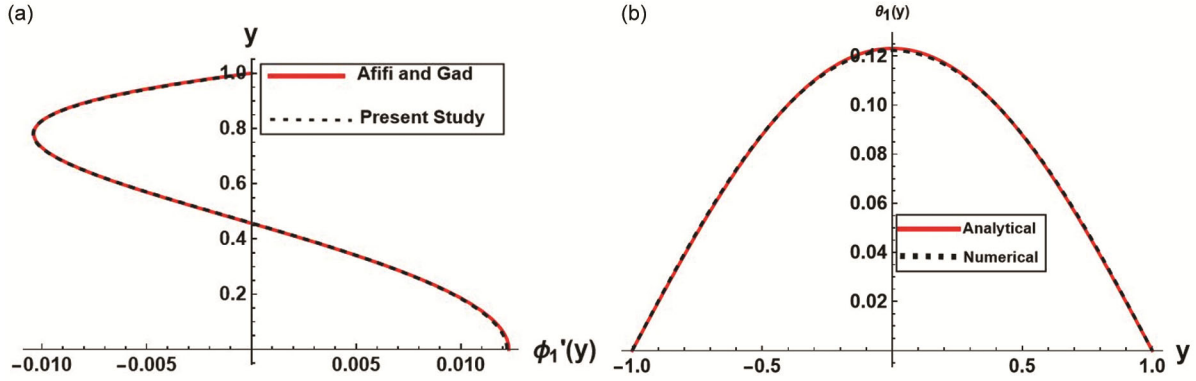

Fig. 10 — Comparative study: (a) Varying velocity distribution and (b) varying temperature for Rd=1, Pr= 7, Re=1, k=1, ξ = −2 and M=0.5

Conclusion

This study explores the thermal behaviour of nanofluid peristaltic transport through a porous medium subjected to a magnetic field and an externally imposed periodic pressure gradient. Using a perturbation expansion with the amplitude ratio as the small parameter, both the steady and oscillatory components of the flow are obtained. The analysis reveals that the first-order solution clearly demonstrates the coupling between peristaltic pumping and pulsatile motion, while the contribution of the steady component also becomes evident in the higher-order corrections when the flow starts from a quiescent state. The key outcomes of this study can be summarized as follows:

- The fluid velocity reduces with a rise in the Hartmann number, whereas it enhances with higher values of the Reynolds number, wave number, permeability parameter, and Grash of number.
- The temperature distribution is enhanced by increases in the permeability parameter, wave number, thermal radiation, heat generation or absorption and Prandtl number, while it diminishes with a rise in the Hartmann number.
- An increase in the Hartmann number diminishes the trapped bolus size, while higher porous parameter, wave number, Grashof number, and Reynolds number promote its enlargement. Among the nanoparticle geometries, cylinder-shaped particles yield the largest bolus, whereas lamina-shaped particles produce the smallest.
- Ag-based nanofluids show higher velocity than Au-based ones. Among the fluids, velocity is highest for the case of water, moderate for kerosene, and lowest for blood due to viscosity differences.
- The velocity field variation of the nanofluid when we apply the different shapes, it is observed that lower shape factor particles exhibit the higher velocities due to reduced drag, while lamina shaped particles slow down the flow compare to remaining three because of larger surface area and higher resistance.
- An increase in thermal radiation, porous parameter, Prandtl number, and Reynolds number enhances heating, whereas a higher Hartmann number reduces the temperature by promoting heat dissipation as evidenced from isothermal contour analysis. Furthermore, the nanoparticle shape also plays a significant role in thermal behaviour. Cylinder-shaped nanoparticles exhibit comparatively lower temperatures within the isothermal contours, while lamina-shaped nanoparticles lead to higher temperature distribution, indicating their stronger thermal enhancement capability.
- The hydrodynamic case can be recovered, from the analysis, of our in the limiting case as M approaches to 0.
- Neglecting nanoparticle effects and considering Gr=0, the current analysis recovers the findings reported by Afifi and Gad[13].

This analytical study evaluates the accuracy of numerical solutions for flow problems that include additional physical effects. Realistic modeling of blood flow in small vessels must incorporate both cardiac-induced pulsatile motion and wall-driven peristaltic transport. Although pulsatile flow is well documented, analytical investigations into the thermal characteristics of peristaltic flow under a periodic pressure gradient are lacking. The results obtained here will contribute significantly to the formulation of mathematical models for addressing complex rheological phenomena.

Acknowledgment

One of the authors (GSSDB) gratefully acknowledges the financial support received in the form of a research scholarship from VIT-AP University, Amaravati-522237, India.

Conflict of Interest

The authors declare that there are no conflicts of interest associated with this work.

Supplementary Information

Supplementary information is available on the website https://nopr.niscpr.res.in/handle/123456789**.**

References

1 Fung Y C, and Yih C S *Peristaltic transport*, (1968) pp 669..
2 Mishra M & Ramachandra R A, Peristaltic transport of a Newtonian fluid in an asymmetric channel, *Z Angew Math Phys*, 54 (2003) 532.
3 Kothandapani M & Srinivas S, Non-linear peristaltic transport of a Newtonian fluid in an inclined asymmetric channel through a porous medium, *Phys Lett A*, 372 (2008) 1265.
4 Srinivas S & Muthuraj R, Peristaltic transport of a Jeffrey fluid under the effect of slip in an inclined asymmetric channel, *Int J Appl Mech*, 2 (2010) 437.
5 Devakar M, Ramesh K & Vajravelu K, Magnetohydrodynamic effects on the peristaltic flow of

couple stress fluid in an inclined tube with endoscope, *J Comput Math Data Sci*, 2 (2022) 100025.

6 Nadeem S & Akbar N S, Effects of heat transfer on the peristaltic transport of MHD Newtonian fluid with variable viscosity: Application of Adomian decomposition method, *Commun Nonlinear Sci Numer Simul*, 14 (2009) 3844.

7 Malathy T & Srinivas S, Pulsating flow of a hydromagnetic fluid between permeable beds, *Int Commun Heat Mass Transf*, 35 (2008) 681.

8 Srinivas S, Kalyan K C & Subramanyam R A, Pulsating flow of Casson fluid in a porous channel with thermal radiation, chemical reaction and applied magnetic field, *Nonlinear Anal Model Control*, 23 (2018) 213.

9 Padma D M & Srinivas S, Thermal characteristics on two immiscible fluid flows in a porous space with time dependent pressure gradient, *Proc Inst Mech Eng Part E: J Mech Eng Sci*, 236 (2022) 2480.

10 Goyal K & Srinivas S, Two-layered magnetohydrodynamics of immiscible pulsatile flow in corrugated curved channel, *Int J Model Simul*, (2024) 1.

11 Srivastava L M & Srivastava V P, Interaction of peristaltic flow with pulsatile flow in a circular cylindrical tube, *J Biomech*, 18 (1985) 247.

12 Usha R & Prema K, Interaction of pulsatile and peristaltic transport induced flows of a particle-fluid suspension, *Z Angew Math Mech*, 78 (1998) 207.

13 Afifi N A & Gad N S, Interaction of peristaltic flow with pulsatile magneto-fluid through a porous medium, *Acta Mech*, 149 (2001) 229.

14 Gad N S, Effect of Hall currents on interaction of pulsatile and peristaltic transport induced flows of a particle-fluid suspension, *Appl Math Comput*, 217 (2011) 4313.

15 Srinivas S, Anasuya J B & Merugu V, Interaction of pulsatile and peristaltic flow of a particle-fluid suspension with thermal effects, *Int Commun Heat Mass Transf*, 163 (2025) 108728.

16 Mekheimer K S, Non-linear peristaltic transport of magnetohydrodynamic flow in an inclined planar channel, *Arab J Sci Eng*, 28 (2003) 183.

17 Srinivas S & Pushparaj V, Non-linear peristaltic transport in an inclined asymmetric channel, *Commun Nonlinear Sci Numer Simul*, 13 (2008) 1782.

18 Nagarani P, Peristaltic transport of a Casson fluid in an inclined channel, *Korea-Aust Rheol J*, 22 (2010) 105.

19 Ramesh K & Devakar M, Magnetohydrodynamic peristaltic transport of couple stress fluid through porous medium in an inclined asymmetric channel with heat transfer, *J Magn Magn Mater*, 394 (2015) 335.

20 Choi S U S, Enhancing thermal conductivity of fluids with nanoparticles, *ASME Int Mech Eng Congr Expo*, (1995) 99.

21 Abbasi F M, Hayat T, Ahmad B & Chen G Q, Slip effects on mixed convective peristaltic transport of copper-water nanofluid in an inclined channel, *PLoS One*, 9 (2014) e105440.

22 Vijayalakshmi A & Srinivas S, A study on hydromagnetic pulsating flow of a nanofluid in a porous channel with thermal radiation, *J Mech*, 33 (2017) 213.

23 Ellahi R, Raza M & Akbar N S, Study of peristaltic flow of nanofluid with entropy generation in a porous medium, *J Porous Media*, 20 (2017) 1.

24 Devaki P, Venkateswarlu B, Srinivas S & Sreenadh S, MHD peristaltic flow of a nanofluid in a constricted artery for different shapes of nanosized particles, *Nonlinear Eng*, 9 (2019) 51.

25 Waqas H, Farooq U, Muhammad T & Manzoor U, Importance of shape factor in Sisko nanofluid flow considering gold nanoparticles, *Alex Eng J*, 61 (2022) 3665.

26 Akbar N S, Habib M B, Rafiq M, Muhammad T & Alghamdi M, Biological structural study of emerging shaped nanoparticles for the blood flow in diverging tapered stenosed arteries to see their application in drug delivery, *Sci Rep*, 14 (2024) 1475.

27 Goyal K & Srinivas S, Pulsatile flow of immiscible ternary hybrid nanofluid in a corrugated curved channel, *Numer Heat Transf Part A: Appl*, 86 (2024) 1.

28 Rashid U, Mawire A, Wang Q, Chamkha A J & Yang K, Finite element and long short-term memory analysis for impact of nanoparticle shape on hybrid nanofluid flow in a lid-driven cavity, *J Comput Des Eng*, 12 (2025) 14.

29 Yih C-S, Instability of unsteady flows or configurations Part 1. Instability of a horizontal liquid layer on an oscillating plane, *J Fluid Mech,* 31 (1968):737.